HHS Public Access

Author manuscript

J Am Chem Soc. Author manuscript; available in PMC 2024 July 05.

Published in final edited form as:

J Am Chem Soc. 2024 May 22; 146(20): 14328–14340. doi:10.1021/jacs.4c03994.

Darobactin Substrate Engineering and Computation Show Radical Stability Governs Ether versus C-C Bond Formation

Austin M. Woodard[1,2], **Francesca Peccati**[3], **Claudio D. Navo**[3], **Gonzalo Jiménez-Osés**[3,4], **Douglas A. Mitchell**[1,2,5,*]

[1]Department of Chemistry, University of Illinois at Urbana-Champaign, Urbana, Illinois 61801, USA.

[2]Carl R. Woese Institute for Genomic Biology, University of Illinois at Urbana-Champaign, Urbana, Illinois 61801, USA.

[3]Center for Cooperative Research in Biosciences (CIC bioGUNE), Basque Research and Technology Alliance (BRTA), Bizkaia Technology Park, Building 801A, 48160 Derio, Spain

[4]Ikerbasque, Basque Foundation for Science, 48013 Bilbao, Spain

[5]Department of Microbiology, University of Illinois at Urbana-Champaign, Urbana, Illinois 61801, USA.

Abstract

The Gram-negative selective antibiotic darobactin A has attracted interest owing to its intriguing fused bicyclic structure and unique targeting of outer membrane protein BamA. Darobactin, a ribosomally synthesized and post-translationally modified peptide (RiPP), is produced by a radical *S*-adenosyl methionine (rSAM)-dependent enzyme (DarE) and contains one ether and one C-C crosslink. Herein, we analyze the enzymatic tolerance and describe an underlying catalytic principle of DarE. These efforts produced 51 enzymatically modified darobactin variants, revealing that DarE can install the ether and C-C crosslinks independently and in different locations on the substrate. Notable variants with fused bicyclic structures were characterized, including darobactin W3Y, with a non-Trp residue at the twice-modified central position, and

[*]**Corresponding Author** Douglas A. Mitchell - Carl R. Woese Institute for Genomic Biology, University of Illinois at Urbana-Champaign, Urbana, Illinois 61801, USA; Department of Chemistry and Department of Microbiology, University of Illinois at Urbana-Champaign, Urbana, Illinois 61801, USA. (douglasm@illinois.edu).

Austin M. Woodard - Carl R. Woese Institute for Genomic Biology, University of Illinois at Urbana-Champaign, Urbana, Illinois 61801, USA

Francesca Peccati – Center for Cooperative Research in Biosciences (CIC bioGUNE), Basque Research and Technology Alliance (BRTA), Bizkaia Technology Park, Building 801A, 48160 Derio, Spain

Claudio D. Navo – Center for Cooperative Research in Biosciences (CIC bioGUNE), Basque Research and Technology Alliance (BRTA), Bizkaia Technology Park, Building 801A, 48160 Derio, Spain

Gonzalo Jiménez-Osés – Center for Cooperative Research in Biosciences (CIC bioGUNE), Basque Research and Technology Alliance (BRTA), Bizkaia Technology Park, Building 801A, 48160 Derio, Spain; Ikerbasque, Basque Foundation for Science, 48013 Bilbao, Spain

Supporting Information

Experimental methods and supporting figures (S1-S97) and tables (S1-S12) (PDF).

Supplemental Dataset 1 contains AlphaFold multimer models (ZIP of PDB coordinate files)

Supplemental Dataset 2 contains a list of bioinformatically identified darobactin precursor sequences (XLSX).

Supplemental Dataset 3 contains a summary of all DarA variant modifications in this study (XLSX).

The authors declare no competing financial interest.

darobactin K5F, which displays a fused diether ring pattern. While lacking antibiotic activity, quantum mechanical modeling of darobactins W3Y and K5F aided in the elucidation of the requisite features for high-affinity BamA engagement. We also provide experimental evidence for β-oxo modification, which adds support for a proposed DarE mechanism. Based on these results, ether and C-C crosslink formation was investigated computationally, and it was determined that more stable and longer-lived aromatic Cβ radicals correlated with ether formation. Further, molecular docking and transition state structures based on high-level quantum mechanical calculations support the different indole connectivity observed for ether (Trp-C7) and C-C (Trp-C6) crosslinks. Finally, mutational analysis and protein structural predictions identified substrate residues that govern engagement to DarE. Our work informs on darobactin scaffold engineering and further unveils the underlying principles of rSAM catalysis.

Graphical Abstract

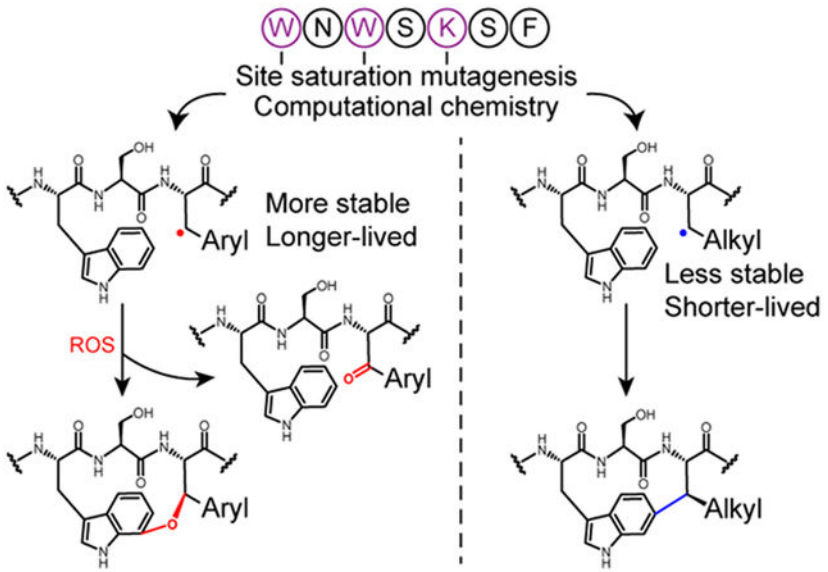

Introduction

The biosynthetic gene clusters (BGCs) for ribosomally synthesized and post-translationally modified peptides (RiPPs) encode a precursor peptide and the cognate modifying enzyme(s). Canonical precursor peptides possess an N-terminal leader region containing a recognition sequence directly engaged by biosynthetic proteins and a C-terminal core region that receives all enzymatic modifications.[1,2] Occasionally, RiPP precursor peptides display a C-terminal follower sequence, which, like the leader region, is not part of the final molecule. Some RiPP BGCs encode peptidases to release unmodified portion(s) of the substrate peptide, while others co-opt proteases encoded elsewhere in the genome.[1-4] Similarly, RiPP BGCs may encode a dedicated transporter for export of the final product.

Structurally intriguing natural products are routinely identified as being formed by radical *S*-adenosylmethionine (rSAM) enzymes, which constitute one of the largest and most diverse enzyme superfamilies (Pfam[5] entry PF04055).[6-8] Within the rSAM active site, an

oxidatively labile [4Fe-4S] center reductively cleaves SAM to produce L-methionine and 5'-deoxyadenosyl radical (5'-dAdo•).[9,10] Hydrogen atom abstraction from the substrate by 5'-dAdo• propagates a radical cascade from which different reaction pathways are available to generate the final product(s).[6,8] As compiled by the web-based repository www.radicalsam.org, ~100,000 rSAM enzymes contain one or more additional [Fe-S] centers and are classified as members of the SPASM/twitch group.[7,11,12] These auxiliary [Fe-S] centers are proposed to aid in substrate alignment and facilitate electron transfer.[13-15] Within RiPP biosynthesis, rSAM enzymes catalyze numerous modifications, including methylation, carbon-carbon and carbon-sulfur crosslinking, epimerization, and more.[2,16-32]

Darobactin A is a twice-cyclized rSAM-modified RiPP (Figure 1).[33] The precursor peptide DarA (NCBI: WP_152962143.1) possesses a heptapeptide core region ($_1$WNWSKSF$_7$) that is modified with two crosslinks: *(i)* an ether (C-O-C) between Trp1-C7 and Trp3-Cβ and *(ii)* a C-C crosslink between Trp3-C6 and Lys5-Cβ. Target identification studies found that darobactin binds to BamA of the β-barrel assembly machinery (BAM) complex, which folds and inserts outer membrane proteins (OMPs) in Pseudomonadota (formerly Proteobacteria).[33-36] Structural data show that darobactin acts as a β-strand mimetic that binds to the lateral gate of BamA analogously to incoming nascent OMPs.[37-41] The strong interaction of darobactin with BamA prevents OMP folding and leads to cell-membrane disruption and bacterial lysis.[33,37,42]

DarE (NCBI: WP_152962147.1) installs both crosslinks onto DarA.[43,44] While precedented, it is rare for a single active site enzyme to catalyze two distinct reaction outcomes on the same substrate (e.g., fructose-1,6-bisphosphate aldolase/phosphatase and a suicide enzyme involved in biotin synthesis in cyanobacteria).[45,46] Recent work has probed the mechanism of crosslink formation by DarE.[47,48] In one proposal, hydrogen abstraction by 5'-dAdo• generates a Trp3-Cβ radical on DarA, which further reacts with molecular oxygen to form a hydroperoxide intermediate. Water was initially proposed as this oxygen source, but this mechanism is now disfavored.[47,49] To form the ether crosslink, either the Trp1 indole can undergo nucleophilic attack to the hydroperoxide intermediate, or the hydroperoxide can undergo homolytic cleavage and addition into the Trp1 indole. An alternative mechanism where hydroxylation of Trp1 precedes ether crosslinking has also been proposed.[47] Formation of the C-C crosslink has been proposed to be similar to SuiB, a rSAM enzyme responsible for streptide maturation, but alternative mechanisms have been proposed.[15,47,49] A more complete understanding of these enzymatic mechanisms will clearly require additional kinetic and spectroscopic evaluation.

Many naturally occurring and engineered darobactin variants have been characterized, which have begun to define the substrate tolerance of DarE. Most of the reported variants, however, involve substitution of the non-modified residues of the DarA core region (i.e., positions 2, 4, 6, 7), which collectively showed minimal impact on forming fused bicyclic products.[38,41,44,49,50] In contrast, less is known about enzymatic tolerance to core positions that are modified (i.e., positions 1, 3, and 5). DarE can tolerate substitution of Lys5 with either Arg or Ala to produce darobactins D and 15, respectively.[38,44,49] Until recently, no experimental data were available regarding the impact of substitutions on DarA core positions 1 and 3. The single tested variant at core position 1 (variant W1F) did not produce

either crosslink; however, when core position 3 was changed to Tyr, His, or Phe, an ether crosslink between core positions 1 and 3 was formed. Similarly, a C-C crosslink formed between core positions 1 and 3 on a W3K variant, suggesting that the crosslink chemistry depended on the residue identity.[48,49] However, no bicyclic variants of darobactin that contain a residue other than Trp at core positions 1 and 3 have been reported. These previous studies provide initial insight into crosslink formation but raise other questions about how and why specific crosslinks form between particular residues.

Here, we describe a combination of experimental and computational analyses to investigate the molecular principles of ether vs. C-C crosslink formation by DarE. Single site-saturation mutagenesis of the three modified core positions indicated that each crosslink could be formed independently of the other and that the location of each crosslink is contingent on the properties of the modified residues. Ether crosslinks form between two aromatic amino acids, while C-C crosslinks form between aromatic and aliphatic amino acids. Immature products with β-oxo amino acids were also characterized, implicating oxygen addition to aromatic residues during ether crosslink formation. Quantum mechanical calculations suggest that the crosslink chemistry is governed by the enhanced longevity of aromatic Cβ radicals over aliphatic Cβ radicals, permitting reaction with an oxygen species. New darobactin variants with two fused ether crosslinks and one with a non-Trp central residue were characterized. Although these variants lacked antibiotic activity, structural analysis identified key geometric features for engineering darobactins to maintain BamA inhibition. Finally, we determined the positions of the DarA leader region that are vital for substrate processing.

Results

DarE Forms the C-C and Ether Crosslinks Independently.

Previous *in vivo* biosynthetic analyses of darobactin have mostly relied on proteolysis and export of mature darobactins by heterologous or native hosts; however, a limitation of most *in vivo* studies is the challenge of detecting biosynthetic intermediates and shunt products.[38,41,44,51] To identify and analyze biosynthetically immature peptides we devised a workflow to reduce endogenous proteolysis of expressed peptides (Figure S1). A co-expression plasmid containing a maltose-binding protein (MBP) fusion to DarA with the Gln-Glu-Ile follower region removed [MBP-DarA(Q8*)] and untagged DarE was constructed. We then performed site-saturation mutagenesis on the three positions modified in DarA (Trp1, Trp3, Lys5) to investigate the substrate tolerance of DarE. After expression in BL21(DE3) *E. coli*, the DarA variants were purified and analyzed by proteolytic digestion and matrix-assisted laser desorption/ionization time-of-flight mass spectrometry (MALDI-TOF-MS) (Figures S2-S4). Glu(−4) of wild-type DarA provided a convenient endoproteinase GluC digestion site that excluded all but three residues of the leader region (Ile-Thr-Ala) and was thus used throughout this study. The Ile-Thr-Ala tripeptide was readily removed from darobactin variants by replacing GluC with proteinase K, as previously described.[47] Structure determination was performed using high-resolution and tandem mass spectrometry (HR-MS/MS), MALDI LIFT-MS/MS, and multidimensional NMR spectroscopy.[52]

The most prevalent DarE-installed modification among the DarA variants was a loss of 2 Da (Figures S2-S4). HR-MS/MS analysis of the −2 Da species of multiple DarA variants (e.g., W1D, W1H, W1N, K5Q, K5S, and K5Y) localized the mass loss to Trp3, consistent with previous studies showing DarE can form α,β-dehydrotryptophan (dhTrp) (Figures S5-S10).[47,49] However, some Trp1 variants (e.g., W1N and W1D) gave very low-intensity daughter ions between Trp3 and Lys5, which in mature darobactin are C-C linked. Given that C-C formation also yields a −2 Da mass loss with hindered MS/MS fragmentation, we performed ultra-high-performance liquid chromatography (UHPLC) of GluC-digested DarA-W1N and -W1D variants (Figures S11-S12). We then analyzed the peptides by HR-MS/MS and site-specific proteolytic digestion to differentiate dhTrp and C-C crosslink formation at core position 3. Trypsin does not cleave after crosslinked Lys5 in darobactin A, and similarly, chymotrypsin does not cleave after crosslinked Trp (Figure S13).[49] For both DarA-W1N and -W1D, the −2 Da species eluted into two distinct HPLC fractions (Figures S11-S12). The earlier eluting −2 Da species was the most abundant product for DarA-W1N and -W1D, with a 23- and 158-fold increase in relative area under the curve compared to the later eluting species, respectively. The earlier eluting −2 Da products lacked HR-MS/MS fragmentation within the Trp3-Lys5 motif and were also recalcitrant to trypsin and chymotrypsin digestion, supporting C-C crosslink formation. HR-MS/MS of the later eluting species localized the modification to Trp3, and these peptides were susceptible to trypsin digestion at Lys5, supporting the absence of the C-C crosslink. We also noticed that dhTrp was not a chymotryptic site (Figures S14-S21).

The formation of a single C-C crosslink was also observed for the Trp3 variants. Indeed, DarA-W3K, -W3N, -W3Q, and -W3R displayed −2 Da modifications that lacked HR-MS/MS fragmentation between core positions 1 and 3 (Figures S22-S25). For instance, the −2 Da modified DarA-W3R variant was not cleaved after Trp1 by chymotrypsin or Arg3 by trypsin (Figure 2). To confirm or refute C-C crosslink formation, we produced a larger quantity of the GluC-digested W3R variant. The resulting peptide, which retains Ile-Thr-Ala from the leader region (Figure 1), was purified by UHPLC (HRMS: $C_{55}H_{84}N_{16}O_{15}^{2+}$, *calc.* $[M+2H]^{2+}$: 604.3146; *obs.* $[M+2H]^{2+}$: 604.3143; error: 0.5 ppm) (Figure S26). Subsequent NMR spectroscopic analysis, specifically ^{1}H-^{1}H TOCSY and ^{1}H-^{13}C HSQC experiments, yielded diagnostic correlations indicating that Arg3-Cβ was monosubstituted (Figures S27-S31). Similarly, Trp1 was assigned as monosubstituted at C6 via ^{1}H-^{1}H TOCSY, ^{1}H-^{13}C HSQC, and ^{1}H-^{1}H NOESY cross-peaks. The NOE correlations between Trp1-C7H with Arg3-CαH/CγH/CδH and Arg3-CβH with Trp1-C5H established a Trp1-C6 and Arg3-Cβ connectivity for the C-C crosslink and suggested an (*S*) configuration for the new stereocenter at Arg3-Cβ (Figure 2). These data show C-C crosslink formation where the ether crosslink is naturally found in darobactin.

Another prevalent modification of DarE-processed DarA variants was a +14 Da mass shift that matched the expected deviation for ether (C-O-C) crosslink formation (Figures S2-S4).[47-49] Previous work has shown that collision-induced dissociation (CID) of the ether crosslink produces distinguishing daughter ions.[38] HR-MS/MS spectra consistent with monoether formation at core positions 1 and 3 were observed for DarA variants W3F, W3H, W3Y, K5F, K5H, K5W, and K5Y (Figures S32-S38). However, the CID spectra for variants K5H, K5Y, and K5W were consistent with an isobaric mixture of monoether formation

at core positions 3 and 5. UHPLC and HR-MS/MS analyses of modified K5H confirmed formation of Trp1-Trp3 (monoether) and Trp3-His5 (monoether) (Figure S36). Analogous to C-C instead of ether installation at core position 1 and 3, an ether can be installed at position 3 and 5 where the C-C crosslink is naturally found in darobactin A. With an understanding of macrocycle type and location, we next investigated if the macrocycle size was adjustable. DarE was intolerant towards macrocycle expansion (i.e., WN**G**WSKSF, WN**GG**WSKSF, WNWS**G**KSF, and WNWS**GG**KSF) and contraction (ΔAsn2 and ΔSer4) (Figures S39-S40).

DarE Generates β-oxo Amino Acids and Formylglycine.

Instead of a −2 Da mass shift resulting from C-C crosslink formation or Trp dehydrogenation, HR-MS/MS of DarA-W3S and -K5S localized a −2 Da modification to Ser3 and Ser5, respectively (Figures S41-S42). Given that DarE is retrieved by TIGR03942 (hidden Markov model), it is homologous to anaerobic sulfatase-maturing enzyme and bears 48% sequence similarity to the enzyme anSMEcpe (NCBI: BAB80341.1).[53-56] Thus, we suspected that DarE may have generated formylglycine at the newly introduced Ser positions. To explore this possibility, DarE-modified and purified DarA-W3S was reacted with *o*-benzylhydroxylamine.[57] Oxime formation at core position 3 was confirmed by LIFT-MS/MS. (Figures S43-S44). Similar results were obtained with variant K5S; however, the low signal intensity of the oxime adduct prevented MS/MS-based confirmation.

Similarly, HR-MS/MS analysis of multiple Trp1 variants with a +14 Da modification localized the mass increase to Trp3 (Figures S45-S48). Instead of ether formation, we suspected conversion to β-oxotryptophan. DarA-W1Y displayed near-complete conversion to the +14 Da species and was selected for further investigation. Labeling of DarA-W1Y with *o*-benzylhydroxylamine was unsuccessful, potentially owing to reduced electrophilicity of the benzylic position. Treatment of DarE-modified DarA-W1Y with 2,4-dinitrophenylhydrazine (2,4-DNPH), however, resulted in hydrazone formation with LIFT-MS/MS localizing the adduct to core position 3 (Figure S49).[52,58,59] DarA variants W3N, K5H, K5R, K5W, and K5Y also contained β-oxotryptophan modifications at core position 3, except for DarA-W3N, where Trp1 was converted to β-oxotryptophan. (Figures S50-S54). We also detected formation of β-oxotyrosine and β-oxohistidine at core position 3 on variants W3Y and W3H, respectively (Figures 3, S55-S56, Table S3).[52] Further, variant K5H displayed β-oxohistidine at position 5 (Figure S57).

Variant W3Y Contains Ether and C-C Crosslinks.

Eight DarA variants exhibited +12 Da modifications, consistent with ether (+14 Da) and C-C (−2 Da) crosslink formation (Figures S2-S4). While no Trp1 variant gave evidence of ether and C-C crosslink formation, variant W3Y yielded a +12 Da product after co-expression with DarE (HRMS after GluC digestion: $C_{58}H_{79}N_{13}O_{17}^{2+}$, *calc*. $[M+2H]^{2+}$: 614.7853; *obs*. $[M+2H]^{2+}$: 614.7839; error: 2.3 ppm) (Figure S58). The DarA-W3Y product was thus scaled up, digested with proteinase K, purified, and characterized by NMR spectroscopy (Figures 3, S59-S64, Table S4). Using ^{1}H-^{1}H TOCSY and ^{1}H-^{13}C HSQC couplings, the characteristic downfield signal, δ_{CH} 5.47/83.6, was assigned to Tyr3-CβH and hence was expected to be involved in an ether crosslink. Similarly, Trp1-C7 was monosubstituted, as evidenced by the absence of ^{1}H-^{1}H TOCSY and ^{1}H-^{1}H NOESY

cross-peaks. In addition, the observed NOE correlations between Trp1-C5H/C6H and Tyr3-CβH, as well as Trp1-NH1 and Tyr3-C6H, indicated ether formation between Trp1-C7 and Tyr3-Cβ (*R* stereochemistry) similar to other darobactins.[33,38] Analogously, ^{1}H-^{1}H TOCSY and ^{1}H-^{13}C HSQC resonances highlighted that Tyr3 featured a *meta* and *para*-disubstituted phenyl substructure (δ_{H6} 6.81, d ≈ 2.3 Hz) and Lys5-Cβ was monosubstituted (Figures 3, S61-S64). The observation of NOE correlations from Tyr3-C2H to Lys5-CβH/amide NH suggested that the C-C crosslink was between Tyr3-C3 and Lys5-Cβ with (*S*) stereochemistry at Lys5-CβH.

DarE Installs Fused Ether and C-C Crosslinks on Multiple Lys5 Variants.

DarE processing of the Lys5 variants yielded seven DarA variants (i.e., K5A, K5F, K5L, K5N, K5Q, K5R, and K5W) with a +12 Da mass shift (Figure S4). Previous research characterized variants K5R (darobactin D) and K5A (darobactin 16) as having ether and C-C crosslinks akin to darobactin A.[38,44] HR-MS/MS of variants K5L, K5N, and K5Q suggested that ether and C-C crosslinks were formed (Figures S65-S67). The yields for darobactins K5L, K5N, and K5Q were too low for structural confirmation by NMR; however, we hypothesize that the crosslinks likely formed with the same connectivity and stereochemistry as in darobactin A.[33] HR-MS/MS of DarA-K5W (+12 Da) indicated Trp1-Trp3 ether formation but was inconsistent with C-C crosslink formation. Rather, the −2 Da modification was localized onto Trp5, consistent with dhTrp (Figure S68).

Aromatic Residues at Core Position 5 Yield Two Ether Crosslinks.

While the +12 Da species from variant K5F gave very low ion intensity, a robust +28 Da modification was observed, suggesting a diether product (Figures 4 and S4). Analysis of variant K5F (+28 Da) supported a molecular formula with net addition of two oxygens and net loss of four hydrogens (HRMS after GluC digestion: $C_{63}H_{76}N_{13}O_{17}^{+}$, *calc*. $[M+H]^{+}$: 1286.5477; *obs*. $[M+H]^{+}$: 1286.5459; error: 1.4 ppm) as well as daughter ions consistent with a fused diether product (Figure S69). Subsequent NMR analysis of proteinase K-digested and UHPLC-purified darobactin K5F confirmed the structure. (Figures 4, S70-S75, Table S5).

Analysis of the ^{1}H-^{13}C HSQC spectrum revealed two discriminative doublet resonances (δ_{CH} 5.9/79.2, 5.52/84.2), assigned as Trp3-CβH and Phe5-CβH, respectively. Assisted by ^{1}H-^{1}H TOCSY and ^{1}H-^{1}H NOESY, we found that the C7 positions of Trp1 and Trp3 were implicated in ether crosslink formation. Specifically, NOE correlations from Trp3-CβH to Trp1-C6H and Phe5-CβH to Trp3-C6H established the locations of the two ether crosslinks. Ultimately, the observed NOEs between Trp1-NH1 and Trp3-CαH alongside Trp3-C6H and Lys5-amide NH elucidated an (*R*) configuration for both new stereocenters (Figures 4, S72-S75).

HR-MS/MS confirmed that variants K5H, K5W, and K5Y similarly displayed two ether crosslinks after DarE processing (Figures S76-S78). Notably, a variant with a single ether crosslink and a β-oxo amino acid would be isobaric (+28 Da) with the same peptide containing two ether crosslinks. For variants K5W and K5Y, evidence of these isobaric species was observed by HR-MS/MS (Figures S77-S78). In both cases, the fragmentation

data always supported ether formation at Trp1-Trp3 but only partial ether formation at core positions 3–5. The remainder of the daughter ions assigned the +14 Da modification to core position 5, consistent with β-oxotryptophan and β-oxotyrosine for variants K5W and K5Y, respectively.

Computational Assessment of Ether Versus C-C Crosslinking.

Armed with DarA variant processing data, we next investigated the factors behind DarE crosslink differentiation. The intrinsic preferences towards ether versus C-C formation were studied quantum mechanically on abbreviated models of unmodified DarA (computational details provided in methods). The models ($\mathbf{A_{Me}H}$ and $\mathbf{A_{Ph}H}$) feature trimmed tripeptides mimicking the amino acid sequences for the second macrocycle (WSX motif): an indole-3-propionic acid, mimicking Trp3; an Ala, mimicking Ser4; and 2-methyl- or 2-phenylethanamine as mimics for β-alkyl (i.e., Lys) and β-aryl (i.e., Phe) amino acids. To eliminate the influence of conformational effects, which are presumably minimal when bound to the DarE active site, models were considered to be in a near-attack conformation similar to that found in atomic-resolution structures of bound darobactin.[37] For transition state calculations, only the reaction leading to the experimentally observed stereochemistry for each crosslink was considered.

First, we evaluated the stability of Cβ-centered radicals as a function of the substituent (alkyl or aryl) on DarA core position 5. Amino acid radical stability is commonly calculated from X-H bond dissociation energies (BDE, X = C, N, O, S) using the isodesmic reaction method.[60,61] Following this approach, we analyzed the thermodynamics of the equilibria between the neutral peptide models and the 5'-dAdo• cofactor ($\mathbf{A_RH}$ + 5'-dAdo• $\mathbf{A_R}$• + 5'-dAdoH), which was exergonic in all cases. The radical $\mathbf{A_{Ph}}$• was calculated to be ~9 kcal mol^{-1} more stable than $\mathbf{A_{Me}}$• ($\Delta G[\mathbf{A_{Ph}}\bullet] = -13.7$ kcal mol^{-1} vs. $\Delta G[\mathbf{A_{Me}}\bullet] = -4.5$ kcal mol^{-1}), resulting in an activation energy for the nucleophilic addition of the radical to Trp3-C6 that is ~5 kcal mol^{-1} higher ($\Delta G^{\ddagger}[\mathbf{A_{Ph}}\bullet\mathbf{\_TS_6}] = 19.8$ kcal mol^{-1} vs. $\Delta G^{\ddagger}[\mathbf{A_{Me}}\bullet\mathbf{\_TS_6}] = 14.9$ kcal mol^{-1}). This energy difference was reflected in the later transition state character of $\mathbf{A_{Ph}}\bullet\mathbf{\_TS_6}$ (C-C forming bond distance 2.09 Å) compared to $\mathbf{A_{Me}}\bullet\mathbf{\_TS_6}$ (C–C forming bond distance 2.16 Å). Translation of activation energies into radical half-lives ($t_{1/2}$) at 25 °C yields $t_{1/2}[\mathbf{A_{Ph}}\bullet] = 37$ s, whereas $t_{1/2}[\mathbf{A_{Me}}\bullet] = 0.009$ s (Figure 5). These results suggest that alkyl Cβ-centered radicals rapidly react to form C-C crosslinks. In contrast, aryl Cβ-centered radicals may persist long enough to engage reactive oxygen species, as proposed for ether crosslink formation in darobactin.[47]

Of note, the type of substituent at core position 5 does not significantly affect the stability of the radical intermediates ($\mathbf{A_R}\bullet\mathbf{\_Int_6}$; $\Delta\Delta G_{Ph\text{-}Me} = 0.5$ kcal mol^{-1}) or the final aromatic products ($\mathbf{A_R}\bullet\mathbf{_Prod_6}$; $\Delta\Delta G_{Ph\text{-}Me} = 1.1$ kcal mol^{-1}), suggesting that the experimentally observed reactivity must be under kinetic control (Figures S79-S80). Therefore, the calculated mechanism is similar to that proposed for the Minisci reaction, which involves a stepwise addition of nucleophilic C-centered radicals to heteroarenes to form a C-C bond (Figure S81).[62,63] Here, we assume that the nucleophilic addition of the radical to the six-membered ring of the indole is rate-limiting. Since the final products are aromatic and thus highly stable ($\Delta G \approx -80$ kcal mol^{-1} with 5'-dAdo• as the presumed radical hydrogen

atom abstractor), a small activation barrier for the subsequent hydrogen abstraction step is expected according to Hammond's postulate; in fact, attempts to locate transition structures using oxygen or carbon radical hydrogen atom abstractors resulted in barrierless, downhill energy profiles.

We then focused on the ether crosslink, which is hypothesized to form from an O-centered alkoxy radical (**O_{Ph}•** and **O_{Me}•**) resulting from the reaction of Cβ-centered radicals (**A_{Ph}•** and **A_{Me}•**) with molecular oxygen followed by homolytic cleavage of the O-O bond.[47] In both cases, the calculated intrinsic activation barriers were significantly lower for aryl over alkyl-substituted alkoxy radicals ($\Delta G^{\ddagger}$[**O_{Ph}•_TS_7**] = 8.3 kcal mol^{-1} vs. $\Delta G^{\ddagger}$[**O_{Me}•_TS_7**] = 9.7 kcal mol^{-1}) leading to half-lives around 0.1–1 μs (Figures 5, S82). Hence, the fact that ether formation is intrinsically faster than C-C bond formation suggests that the chemoselectivity observed for aromatic amino acids at core position 5 to form ether crosslinks must arise from the higher stability of their initial Cβ-centered radicals.

Ether crosslink formation was also analyzed using phenol and phenoxide substituents to mimic neutral and deprotonated Tyr5 (**O_{PhOH}•** and **O_{PhO^-}•**, respectively). The activation barrier increases for the phenoxide surrogate due to the higher delocalization of the spin density ($\Delta G^{\ddagger}$[**O_{PhO^-}•_TS_7**] = 10.6 kcal mol^{-1}) (Figures 5, S83). This increase in the activation barrier is even more dramatic when the environmental dielectric constant in the calculations is changed from water (ε=78) to lower values often used to mimic the polarity inside the active sites of typical enzymes (ε=4),[64,65] where the basic O-centered radical can deprotonate the indole NH ($\Delta G^{\ddagger}$[**O_{PhO^-}•_TS_7'**] = 35.1 kcal mol^{-1}) (Figure S84). Altogether, these results support the experimentally observed formation of β-oxotyrosine as a competitive pathway to ether crosslinking.

Finally, the observed change in the regioselectivity of ether versus C-C crosslinking to give reactions at C6 or C7 of Trp, respectively, was also calculated for **O_{Ph}•**. In the case of the experimentally observed addition to C7, the backbone displayed an extended β-sheet-like conformation in the transition state (**O_{Ph}•_TS_7**) (Figure 5). However, for addition to C6, up to three different transition state conformations with different backbone geometries (polyproline-II, β-sheet, and inverse γ-turn) but similar energies were calculated (**O_{Ph}•_$TS_{6a\text{-}c}$**; $\Delta\Delta G^{\ddagger}_{TS6\text{-}TS7} \approx -0.4$ to +1.3 kcal mol^{-1} assuming Curtin-Hammet conditions). These three conformationally distinct pathways converge to the same aromatic product after hydrogen atom abstraction (Figures S85-S86). Although the similar energies of the regiodivergent transition states could make the formation of both products competitive, molecular docking calculations show significant differences in the preferred binding poses of extended models of those transition states to DarE (computational details provided in methods) (Figure S87, Table S8). **O_{Ph}•_TS_{7ext}** binds to DarE with the highest score and places the alkoxy radical closest to the 5'-dAdoH cofactor. This binding mode is stabilized by multiple interactions, including a hydrogen bond between DarA-Ser4 side chain and the cofactor adenine (Figure 5). Additionally, numerous polar residues of DarE (i.e., Glu250, Arg298, Asp316, and Tyr318) engage the DarA-Asn2 side chain while DarE-Asp340 and -His123 stabilize the DarA-Trp3 side chain through hydrogen bonding and π-stacking. These results suggest that DarE enhances the slight innate preference towards ether crosslinking at C7 by binding DarA in a near-attack, extended conformation. The

preference for ether crosslinking at C7 is further corroborated by a slightly higher binding affinity of the observed regioisomer **OPh_Prod$_{7ext}$** calculated with MM/GBSA simulations (Table S8).

Biological Activity Assessment.

None of the tested variants (i.e., DarA W3R, darobactin W3Y, and darobactin K5F) were growth suppressive up to 32 μg/mL against *E. coli* K-12 MG1655. Variant W3R displayed a single crosslink and retained the Ile-Thr-Ala motif from the leader region; thus, the rigidity and ability to pre-organize into a β-strand for proper alignment with BamA was expectedly impacted (Figure 2).[37] Conversely, darobactins W3Y and K5F are considered mature, as both are bicyclic and do not retain any leader or follower residues (Figures 3-4). We surmised that the altered residues and linkages caused an unfavorable distortion of the β-strand-like structure, preventing proper alignment with BamA. To investigate this possibility, the atomic-resolution crystallographic structure of darobactin A bound to BamA was compared with computationally modeled darobactins A, W3Y, and K5F (Figure S88). We focused on the individual and overall macrocyclic widths, which define the locations of atoms involved in H-bonding between darobactin and BamA. Measured from darobactin A bound to BamA (PDB: 7NRE), the Trp1-Cα to Trp3-Cα (**D1**), Trp3-Cα to Lys5-Cα (**D2**), and Trp1-Cα to Lys5-Cα (**D3**) distances are 6.78 Å, 6.81 Å, and 13.52 Å, respectively.[37] Since we lack atomic-resolution structures of the new darobactin variants bound to BamA, we modeled darobactin A and performed molecular optimization with quantum mechanics *in silico*. The obtained values for **D1-D3** were 6.91 Å, 6.87 Å, and 13.72 Å, respectively, and permit a more direct comparison to the same measurements on the new variants.

Accordingly, darobactins W3Y and K5F were modeled and quantum mechanically optimized *in silico* using NMR-determined stereochemical information. While **D1** for darobactin W3Y (6.90 Å) was identical to darobactin A, the **D2** and **D3** values were significantly shorter (6.02 Å and 12.90 Å, respectively) as expected due to the reduced size of the second macrocycle (Table S11). When darobactin W3Y was overlaid onto darobactin A bound to BamA, the atoms involved in H-bonding on the C-terminus of darobactin W3Y were offset from those observed with darobactins A and B likely disrupting and interaction with BamA (Figure S89-S90). The **D1** and **D2** values for darobactin K5F were in closer agreement with darobactin A (6.87 Å and 6.92 Å); however, **D3** was slightly shorter (13.56 Å) (Figure S88, Table S11).

Another consideration for BamA engagement would be maintenance of the ideal extended conformation for proper β-sheet formation with the lateral gate of BamA. Crystallographically derived and *in silico* modeled darobactins A and B have minimal peptide backbone curvature as expected for a β-strand mimetic (Figure S88). While darobactin W3Y also had minimal backbone curvature, darobactin K5F exhibited significant curvature. When darobactin K5F was overlaid onto darobactin A bound to BamA (PDB: 7NRE), it was evident that the H-bond distances between darobactin K5F and β1 of BamA were perturbed compared to darobactin A and B. Notably, the H-bonding distances at the C-terminus of darobactin K5F were 1.0–1.5 Å longer compared to darobactins A and B (Figures S89-S90). To investigate backbone curvature more thoroughly, dihedral angles were

calculated for core positions 2–5 for all indicated darobactins (Table S12). As expected, the dihedral angles for Asn2, which is within an identical ether motif for each analyzed darobactin, did not vary significantly among the *in silico* modeled and crystallographically derived darobactin variants except for the ψ angle, which was around 30° larger for the *in silico* darobactins (Table S12). At core position 4, however, the ω angle for darobactin K5F is 14–24° smaller than all other darobactins and thus contributes to the observed curvature. This is likely due to accommodating the additional ether crosslink in darobactin K5F with the Trp3 indole side chain tucked further underneath the backbone than with darobactins A and B. Further, the ψ angle at core position 4 for darobactins W3Y and K5F are 30° smaller and 10–30° larger, respectively, than darobactins A and B, compounding the structural deviation (Table S12). While more high-resolution structural data would strengthen these trends, we encourage the use of such modeling measurements in future darobactin engineering efforts.

Assessment of the DarA Leader Region Identifies Critical and Dispensable Regions.

Previous work has evaluated the mechanism and substrate scope of DarE; however, the leader region of DarA has not yet been investigated. The darobactin BGC lacks a RiPP Recognition Element (RRE) commonly used for substrate binding; however, RRE-independent RiPPs are well known.[2,66,67] DarE has an N-terminal extension of ~60 residues before the rSAM domain, which could serve the same purpose as an RRE. AlphaFold multimer structures composed of multiple darobactin maturases show that the cognate precursor peptides wrap around the N-terminal lobe of the darobactin synthase before entering the active site (Figure S91, Supplemental Dataset 1).[68] Removal of residues 1–60 from DarE abolished processing (Figure S92).

To evaluate the contribution of the leader region to DarE processing, upwards of 30 residues were removed from the N-terminus of DarA with a truncation step size of 5 amino acids. These truncated constructs were then co-expressed with DarE (Figure 6). As unmodified DarA was highly susceptible to endogenous proteolytic degradation in *E. coli*, the series of N-terminal truncations to the DarA leader region were co-expressed with DarE at colder temperatures and slower shaking. Further, we found that retaining the wild-type Gln-Glu-Ile tripeptide follower sequence of DarA aided in the detection of unmodified peptides. Removal of the first 5 and 10 residues of DarA had little effect on processing by DarE, while removal of the first 15 residues led to a more pronounced processing deficit, as assessed by MS (observation of the +12 Da species). DarE processing of DarA was nearly abolished after removal of the first 20 residues of DarA. This consequential region of DarA contains multiple highly conserved residues, which may be recognized by DarE and thus explain the loss of processing (Figure 6, Supplemental Dataset 2). To evaluate the contribution of conserved residues of the DarA leader region, we prepared six individual Ala-substituted variants and performed co-expression with DarE in *E. coli*. Variants S(−32)A, L(−31)A, and F(−27)A displayed significantly reduced processing while the L(−34)A, S(−28)A, and K(−26)A variants exhibited much more minor effects on DarA processing (Figure 6). The AlphaFold multimer[68,69] predicted structure of DarA and DarE places Leu(−31) and Phe(−27) into conserved hydrophobic pockets of DarE[70] while Ser(−32) may engage DarE through polar interactions (Figure S93, Supplemental Dataset 1).

The sequence logo of bioinformatically identified DarA precursor peptides (see methods) indicates that the next best-conserved portion of the DarA leader region is the Ile-Thr-Ala(−1) motif (Figure 6). To assess the relative importance of this portion of DarA, we prepared several constructs, co-expressed the DarA variants with DarE, and evaluated processing by MALDI-TOF-MS. While the I(−3)A variant resulted in minimal change to DarA processing, the T(−2)A variant was significantly decreased in processing (Figure S94). The T(−2)V variant was fully processed while the T(−2)S variant was diminished; therefore, we hypothesize that Thr(−2) plays a pivotal role in correctly orientating the DarA core region in the DarE active site (Figure S95). Variants that shift the register of Thr(−2) (IT**A**AWNWSKSF and I**A**TAWNWSKSF) support this notion based on DarE processing (Figure S94). While atomic-resolution validation will require additional investigation, this work delineates the specific positions of the DarA leader region that engender processing by DarE.

Discussion

The rSAM enzyme DarE uniquely installs ether (C-O-C) and C-C crosslinks on DarA (Figure 1). To investigate the substrate tolerance and gain insights into the mechanism of DarE and the structure-activity relationship of BamA inhibition, we generated 63 darobactin variants and 16 leader region variants of DarA. Among the constructed darobactin variants, 51 contained at least one DarE-dependent modification, while 10 variants possessed a bicyclic structure analogous to mature darobactin. A noticeable facet of the different variants we analyzed is the installation of ether crosslinks between aromatic amino acids, while C-C crosslinks formed between an aromatic and a non-aromatic amino acid. Further, the processing outcomes of the DarA variants disclosed here demonstrate that neither crosslink is a prerequisite to form the other, and that crosslinks can be formed at non-canonical core positions (i.e., C-C at positions 1–3 and ether at positions 3–5). Taken together with the results of site-saturation mutagenesis at core positions 1, 3, and 5, as well as formylglycine generation in certain variants, we conclude that the DarE-catalyzed reaction is under substrate control, akin to other RiPP-processing enzymes[71-78] and recently published research on the darobactin family of natural products.[48]

While several DarA variants produced in our work resulted in a fused diether product, the Zhang group identified a natural darobactin-like product from *Rhizobium sullae* displaying two discrete ether crosslinks.[48] Under our co-expression conditions, DarE did not tolerate DarA variants that would form a discrete pattern of ether crosslinks, underscoring the nuances of coevolution of darobactin synthases and their cognate substrate peptides. It remains possible that natural darobactin-like compounds possess fused diether rings, given the genomic identification of core sequences that contain aromatic residues at core position 5 (e.g., WNWS**F**RF and WRWS**W**PF).[27]

To better understand ether versus C-C crosslink formation, we performed extensive quantum mechanical calculations and enzyme docking studies. Previous theoretical analyses have investigated rSAM enzyme mechanisms, and our studies illustrate how substrate radical stability and transition state structure correlates with the DarE reaction outcome.[79-81] We acknowledge that the QM calculations presented are somewhat limited, as they

focus exclusively on the near-attack conformation of the substrates and do not account for the role of DarE in fine-tuning the crosslink differentiation preferences of DarA variants. A comprehensive description would account for the flexibility of the DarA, DarE, SAM, as well as the full network of solvent interactions for the entire reaction coordinate. Accurate accounting for these effects is virtually impossible with the existing computational techniques; thus, we followed a minimalistic approach grounded in a robust theoretical framework that qualitatively explains the crosslink differentiation preferences. Notwithstanding the computational limitations, insights from this study should allow the rational engineering of darobactin variants, and perhaps any rSAM-installed cyclophane, to contain a desired crosslink type. Such knowledge could be crucial, given that subtle differences in macrocycle diameter and geometry can vastly perturb the resulting biological activity.

Many natural and artificial darobactin analogs have been reported. These include an intriguing case where Trp1 is naturally brominated, which displays improved activity towards clinically relevant pathogens.[51] Although none of the variants we tested were growth-suppressive towards *E. coli*, we were able to explain why the structures limited activity based on quantum mechanical structure optimization. The perturbations to the macrocyclic structure of darobactin A provide orthogonal insight into the requisite features of high affinity binding to BamA. This includes guidance on individual macrocycle diameters, overall fused macrocycle widths, proper peptide backbone curvature, and optimal dihedral angles. These geometric attributes were used to evaluate the β-strand conformation of active and inactive darobactins with respect to BamA alignment. Our analysis indicated that backbone curvature should be minimal and that the ω dihedral angle at core position 4 contributes significantly to the extent of backbone curvature. Inactive molecules are critical for understanding SAR, and our results provide valuable insight into the requirements for BamA binding and can be used to design and evaluate future darobactin variants. In addition, future efforts may consider producing an N-terminal extension of darobactin that would enter the lumen of BamA (akin to dynobactin) while maintaining a fused ring pattern to retain conformational rigidity and thus high affinity for the lateral gate.[27]

Another benefit resulting from our DarA mutational analysis is additional information on the enzymatic mechanism of ether and C-C crosslink formation. Specifically, our workflow was designed to permit the characterization of biosynthetically immature products. In a previously proposed ether crosslink mechanism, an alkoxy radical intermediate on Trp3-Cβ is postulated to form.[47] When conditions are inadequate for ether formation, the alkoxy radical may produce β-oxotryptophan. We observed multiple DarA variants containing β-oxotryptophan, β-oxotyrosine, or β-oxohistidine, supporting oxygen addition to Cβ of the C-terminal residue undergoing crosslink formation. A particularly informative DarA variant was W3Y, which formed three distinct products upon co-expression with DarE: *(i)* Trp1-Tyr3 ether and Tyr3-Lys5 C-C (fused bicyclic), *(ii)* Trp1-Tyr3 ether (single macrocycle), and *(iii)* β-oxotyrosine at position 3 (no macrocycle). Of the three modified DarA-W3Y species, the bicyclic product was the least abundant, while the single ether crosslink and β-oxotyrosine products were 2.7x and 7.5x more abundant, respectively, based on UHPLC purification. Our interpretation is that each product originated from an initial alkoxy radical that proceeded down diverging pathways to what was ultimately detected. Clearly, DarE

struggles to process the W3Y variant, and the presumed reduced rate of processing led to enhanced detection of biosynthetically immature and/or shunt products as suggested by computational analysis. On one hand, these results suggest that the ether ring may form first; however, the fact that DarE can install the crosslinks independently prevents a firm conclusion from being made at the present time. Irrespective of ring installation order, our data oppose a mechanism for DarE where Trp1 is first hydroxylated.[47] Instead, our data align well with alkoxy radical formation at Trp3 during ether crosslink mechanism.

While the above analysis provides new insights into the core region of DarA, the processing of canonical RiPP precursor peptides is driven by interaction with the leader region. While DarE does not possess an RRE, the first ~60 amino acids of DarE were predicted to be involved in precursor binding according to AlphaFold multimer predictions and lack of DarA processing upon ablation of DarE(1–60).[66,68] The DarA leader peptide was subjected to a series of truncations, which found that the first 15 amino acids of DarA are largely dispensable for DarE processing. Mutational analysis revealed several residues in the central region of the leader, specifically positions (−32), (−31), and (−27) that were crucial for processing. Similarly, Thr(−2) was identified as a key residue for DarA processing. Intriguingly, lasso peptides, an unrelated RiPP class, also have a highly conserved Thr(−2) residue that is critical for biosynthetic maturation.[82] This may point to a broader trend of β-branched aliphatic residues immediately before the core region to facilitate active site engagement. For this trend to be confirmed or refuted, additional investigation is required.

Conclusions

Research into the mechanisms and capabilities of rSAM enzymes is rapidly progressing. In this study, we uncover the fundamental principles of crosslink formation by the darobactin synthase DarE. Like other RiPP biosynthetic enzymes, DarE is under substrate control with ether and C-C formation determined by the identity of the residues being crosslinked. The computational aspects of this study determined that aromatic residues enable ether over C-C crosslink formation due to increased radical stability and longevity that permits interaction with reactive oxygen species, possibly triplet oxygen. Further, molecular docking and transition state structural calculations provide a rationale for the different connectivity for the ether (Trp-C7) and C-C (Trp-C6) crosslinks. Characterized immature products provide further mechanistic insight into DarE and directly implicate oxygen addition at the Cβ position of residue 3 in the macrocycle forming motif. Along with the mechanism, substrate-enzyme binding was investigated. DarE binds to DarA in an RRE-independent manner, and our work uncovers multiple residues critically involved in the interaction. In summary, the combined experimental and computational analyses disclosed within explain the principles underlying crosslink differentiation and should enhance rational engineering efforts on darobactin-like scaffolds.

Supplementary Material

Refer to Web version on PubMed Central for supplementary material.

Acknowledgments

We thank Sangeetha Ramesh and Timothy Precord for HR-MS/MS data acquisition and Mayuresh Gadgil and Hamada Saad for UHPLC and NMR assistance. We further acknowledge helpful discussions with Prof. David Sarlah, Taras Pogorelov, and Lingyang Zhu. Shravan Dommaraju and Hamada Saad assisted in manuscript proofreading. This work was supported in part by the National Institutes of Health (R01GM123998 to DAM) and by MCIN/AEI/10.13039/501100011033 (PID2021–125946OB-I00 to G.J.O., CEX2021–001136-S to CIC bioGUNE and IJC2020–045506-I to F.P.)

References

(1). Arnison, PG; Bibb MJ; Bierbaum G; Bowers AA; Bugni TS; Bulaj G; Camarero JA; Campopiano DJ; Challis GL; Clardy J; Cotter PD; Craik DJ; Dawson M; Dittmann E; Donadio S; Dorrestein PC; Entian K-D; Fischbach MA; Garavelli JS; Göransson U; Gruber CW; Haft DH; Hemscheidt TK; Hertweck C; Hill C; Horswill AR; Jaspars M; Kelly WL; Klinman JP; Kuipers OP; James Link A; Liu W; Marahiel MA; Mitchell DA; Moll GN; Moore BS; Müller R; Nair SK; Nes IF; Norris GE; Olivera BM; Onaka H; Patchett ML; Piel J; Reaney MJT; Rebuffat S; Paul Ross R; Sahl H-G; Schmidt EW; Selsted ME; Severinov K; Shen B; Sivonen K; Smith L; Stein T; Süssmuth RD; Tagg JR; Tang G-L; Truman AW; Vederas JC; Walsh CT; Walton JD; Wenzel SC; Willey JM; van der Donk WA. Ribosomally Synthesized and Post-Translationally Modified Peptide Natural Products: Overview and Recommendations for a Universal Nomenclature. Nat. Prod. Rep 2013, 30 (1), 108–160. 10.1039/C2NP20085F. [PubMed: 23165928]

(2). Montalbán-López M; Scott TA; Ramesh S; Rahman IR; van Heel AJ; Viel JH; Bandarian V; Dittmann E; Genilloud O; Goto Y; Burgos MJG; Hill C; Kim S; Koehnke J; Latham JA; Link AJ; Martínez B; Nair SK; Nicolet Y; Rebuffat S; Sahl H-G; Sareen D; Schmidt EW; Schmitt L; Severinov K; Süssmuth RD; Truman AW; Wang H; Weng J-K; van Wezel GP; Zhang Q; Zhong J; Piel J; Mitchell DA; Kuipers OP; van der Donk WA New Developments in RiPP Discovery, Enzymology and Engineering. Nat. Prod. Rep 2021, 38 (1), 130–239. 10.1039/D0NP00027B. [PubMed: 32935693]

(3). Ongpipattanakul C; Nair SK Biosynthetic Proteases That Catalyze the Macrocyclization of Ribosomally Synthesized Linear Peptides. Biochemistry 2018, 57 (23), 3201–3209. 10.1021/acs.biochem.8b00114. [PubMed: 29553721]

(4). Eslami SM; van der Donk WA Proteases Involved in Leader Peptide Removal during RiPP Biosynthesis. ACS Bio Med Chem Au 2024, 4 (1), 20–36. 10.1021/acsbiomedchemau.3c00059.

(5). Mistry J; Chuguransky S; Williams L; Qureshi M; Salazar GA; Sonnhammer ELL; Tosatto SCE; Paladin L; Raj S; Richardson LJ; Finn RD; Bateman A Pfam: The Protein Families Database in 2021. Nucleic Acids Res. 2020, 49 (D1), D412–D419. 10.1093/nar/gkaa913.

(6). Broderick JB; Duffus BR; Duschene KS; Shepard EM Radical S-Adenosylmethionine Enzymes. Chem. Rev 2014, 114 (8), 4229–4317. 10.1021/cr4004709. [PubMed: 24476342]

(7). Oberg N; Precord TW; Mitchell DA; Gerlt JA RadicalSAM.Org: A Resource to Interpret Sequence-Function Space and Discover New Radical SAM Enzyme Chemistry. ACS Bio Med Chem Au 2022, 2 (1), 22–35. 10.1021/acsbiomedchemau.1c00048.

(8). Nicolet Y. Structure–Function Relationships of Radical SAM Enzymes. Nat. Catal 2020, 3 (4), 337–350. 10.1038/s41929-020-0448-7.

(9). Bruska MK; Stiebritz MT; Reiher M. Analysis of Differences in Oxygen Sensitivity of Fe–S Clusters. Dalton Trans. 2013, 42 (24), 8729–8735. 10.1039/C3DT50763G. [PubMed: 23632881]

(10). Hoffman BM; Broderick WE; Broderick JB Mechanism of Radical Initiation in the Radical SAM Enzyme Superfamily. Annu. Rev. Biochem 2023, 92 (1), 333–349. 10.1146/annurev-biochem-052621-090638. [PubMed: 37018846]

(11). Grell TAJ; Goldman PJ; Drennan CL SPASM and Twitch Domains in S-Adenosylmethionine (SAM) Radical Enzymes. J. Biol. Chem 2015, 290 (7), 3964–3971. 10.1074/jbc.R114.581249. [PubMed: 25477505]

(12). Haft DH; Basu MK Biological Systems Discovery In Silico: Radical S-Adenosylmethionine Protein Families and Their Target Peptides for Posttranslational Modification. J. Bacteriol 2011, 193 (11), 2745–2755. 10.1128/JB.00040-11. [PubMed: 21478363]

(13). Grove TL; Himes PM; Hwang S; Yumerefendi H; Bonanno JB; Kuhlman B; Almo SC; Bowers AA Structural Insights into Thioether Bond Formation in the Biosynthesis of Sactipeptides. J. Am. Chem. Soc 2017, 139 (34), 11734–11744. 10.1021/jacs.7b01283. [PubMed: 28704043]

(14). Rush KW; Eastman KAS; Kincannon WM; Blackburn NJ; Bandarian V Peptide Selenocysteine Substitutions Reveal Direct Substrate–Enzyme Interactions at Auxiliary Clusters in Radical S-Adenosyl-l-Methionine Maturases. J. Am. Chem. Soc 2023, 145 (18), 10167–10177. 10.1021/jacs.3c00831. [PubMed: 37104670]

(15). Balo AR; Caruso A; Tao L; Tantillo DJ; Seyedsayamdost MR; Britt RD Trapping a Cross-Linked Lysine–Tryptophan Radical in the Catalytic Cycle of the Radical SAM Enzyme SuiB. Proc. Natl. Acad. Sci 2021, 118 (21), e2101571118. 10.1073/pnas.2101571118. [PubMed: 34001621]

(16). Mendauletova A; Kostenko A; Lien Y; Latham J How a Subfamily of Radical S-Adenosylmethionine Enzymes Became a Mainstay of Ribosomally Synthesized and Post-Translationally Modified Peptide Discovery. ACS Bio Med Chem Au 2022, 2 (1), 53–59. 10.1021/acsbiomedchemau.1c00045.

(17). Benjdia A; Balty C; Berteau O Radical SAM Enzymes in the Biosynthesis of Ribosomally Synthesized and Post-Translationally Modified Peptides (RiPPs). Front. Chem 2017, 5, 87. 10.3389/fchem.2017.00087. [PubMed: 29167789]

(18). Clark KA; Bushin LB; Seyedsayamdost MR RaS-RiPPs in Streptococci and the Human Microbiome. ACS Bio Med Chem Au 2022, 2 (4), 328–339. 10.1021/acsbiomedchemau.2c00004.

(19). Clark KA; Seyedsayamdost MR Bioinformatic Atlas of Radical SAM Enzyme-Modified RiPP Natural Products Reveals an Isoleucine–Tryptophan Crosslink. J. Am. Chem. Soc 2022, 144 (39), 17876–17888. 10.1021/jacs.2c06497. [PubMed: 36128669]

(20). Nguyen TQN; Tooh YW; Sugiyama R; Nguyen TPD; Purushothaman M; Leow LC; Hanif K; Yong RHS; Agatha I; Winnerdy FR; Gugger M; Phan AT; Morinaka BI Post-Translational Formation of Strained Cyclophanes in Bacteria. Nat. Chem 2020, 12 (11), 1042–1053. 10.1038/s41557-020-0519-z. [PubMed: 32807886]

(21). Sugiyama R; Suarez AFL; Morishita Y; Nguyen TQN; Tooh YW; Roslan MNHB; Lo Choy J; Su Q; Goh WY; Gunawan GA; Wong FT; Morinaka BI The Biosynthetic Landscape of Triceptides Reveals Radical SAM Enzymes That Catalyze Cyclophane Formation on Tyr- and His-Containing Motifs. J. Am. Chem. Soc 2022, 144 (26), 11580–11593. 10.1021/jacs.2c00521. [PubMed: 35729768]

(22). Morinaka BI; Vagstad AL; Helf MJ; Gugger M; Kegler C; Freeman MF; Bode HB; Piel J Radical S-Adenosyl Methionine Epimerases: Regioselective Introduction of Diverse D-Amino Acid Patterns into Peptide Natural Products. Angew. Chem. Int. Ed 2014, 53 (32), 8503–8507. 10.1002/anie.201400478.

(23). Kincannon WM; Bandarian V 5.20 - Radical SAM Enzymes Involved in Modifications of RiPP Natural Products. In Comprehensive Natural Products III; Liu H.-W. (Ben), Begley TP, Eds.; Elsevier: Oxford, 2020; pp 489–519. 10.1016/B978-0-12-409547-2.14858-9.

(24). Mahanta N; Hudson GA; Mitchell DA Radical S-Adenosylmethionine Enzymes Involved in RiPP Biosynthesis. Biochemistry 2017, 56 (40), 5229–5244. 10.1021/acs.biochem.7b00771. [PubMed: 28895719]

(25). Bushin LB; Covington BC; Clark KA; Caruso A; Seyedsayamdost MR Bicyclostreptins Are Radical SAM Enzyme-Modified Peptides with Unique Cyclization Motifs. Nat. Chem. Biol 2022, 18 (10), 1135–1143. 10.1038/s41589-022-01090-8. [PubMed: 35953547]

(26). Lee H; van der Donk WA Macrocyclization and Backbone Modification in RiPP Biosynthesis. Annu. Rev. Biochem 2022, 91 (1), 269–294. 10.1146/annurev-biochem-032620-104956. [PubMed: 35303785]

(27). Miller RD; Iinishi A; Modaresi SM; Yoo B-K; Curtis TD; Lariviere PJ; Liang L; Son S; Nicolau S; Bargabos R; Morrissette M; Gates MF; Pitt N; Jakob RP; Rath P; Maier T; Malyutin AG; Kaiser JT; Niles S; Karavas B; Ghiglieri M; Bowman SEJ; Rees DC; Hiller S; Lewis K Computational Identification of a Systemic Antibiotic for Gram-Negative Bacteria. Nat. Microbiol 2022, 7 (10), 1661–1672. 10.1038/s41564-022-01227-4. [PubMed: 36163500]

(28). Kostenko A; Lien Y; Mendauletova A; Ngendahimana T; Novitskiy IM; Eaton SS; Latham JA Identification of a Poly-Cyclopropylglycine–Containing Peptide via Bioinformatic

Mapping of Radical S-Adenosylmethionine Enzymes. J. Biol. Chem 2022, 298 (5). 10.1016/j.jbc.2022.101881.

(29). Ma S; Chen H; Li H; Ji X; Deng Z; Ding W; Zhang Q Post-Translational Formation of Aminomalonate by a Promiscuous Peptide-Modifying Radical SAM Enzyme. Angew. Chem. Int. Ed 2021, 60 (36), 19957–19964. 10.1002/anie.202107192.

(30). Clark KA; Covington BC; Seyedsayamdost MR Biosynthesis-Guided Discovery Reveals Enteropeptins as Alternative Sactipeptides Containing N-Methylornithine. Nat. Chem 2022, 14 (12), 1390–1398. 10.1038/s41557-022-01063-3. [PubMed: 36316408]

(31). Phan C-S; Morinaka BI A Prevalent Group of Actinobacterial Radical SAM/SPASM Maturases Involved in Triceptide Biosynthesis. ACS Chem. Biol 2022, 17 (12), 3284–3289. 10.1021/acschembio.2c00621. [PubMed: 36454686]

(32). Lewis JK; Jochimsen AS; Lefave SJ; Young AP; Kincannon WM; Roberts AG; Kieber-Emmons MT; Bandarian V New Role for Radical SAM Enzymes in the Biosynthesis of Thio(Seleno)Oxazole RiPP Natural Products. Biochemistry 2021, 60 (45), 3347–3361. 10.1021/acs.biochem.1c00469. [PubMed: 34730336]

(33). Imai Y; Meyer KJ; Iinishi A; Favre-Godal Q; Green R; Manuse S; Caboni M; Mori M; Niles S; Ghiglieri M; Honrao C; Ma X; Guo JJ; Makriyannis A; Linares-Otoya L; Böhringer N; Wuisan ZG; Kaur H; Wu R; Mateus A; Typas A; Savitski MM; Espinoza JL; O'Rourke A; Nelson KE; Hiller S; Noinaj N; Schäberle TF; D'Onofrio A; Lewis K A New Antibiotic Selectively Kills Gram-Negative Pathogens. Nature 2019, 576 (7787), 459–464. 10.1038/s41586-019-1791-1. [PubMed: 31747680]

(34). Gu Y; Li H; Dong H; Zeng Y; Zhang Z; Paterson NG; Stansfeld PJ; Wang Z; Zhang Y; Wang W; Dong C Structural Basis of Outer Membrane Protein Insertion by the BAM Complex. Nature 2016, 531 (7592), 64–69. 10.1038/nature17199. [PubMed: 26901871]

(35). Wu R; Bakelar JW; Lundquist K; Zhang Z; Kuo KM; Ryoo D; Pang YT; Sun C; White T; Klose T; Jiang W; Gumbart JC; Noinaj N Plasticity within the Barrel Domain of BamA Mediates a Hybrid-Barrel Mechanism by BAM. Nat. Commun 2021, 12 (1), 7131. 10.1038/s41467-021-27449-4. [PubMed: 34880256]

(36). Tomasek D; Kahne D The Assembly of β-Barrel Outer Membrane Proteins. Curr. Opin. Microbiol 2021, 60, 16–23. 10.1016/j.mib.2021.01.009. [PubMed: 33561734]

(37). Kaur H; Jakob RP; Marzinek JK; Green R; Imai Y; Bolla JR; Agustoni E; Robinson CV; Bond PJ; Lewis K; Maier T; Hiller S The Antibiotic Darobactin Mimics a β-Strand to Inhibit Outer Membrane Insertase. Nature 2021, 593 (7857), 125–129. 10.1038/s41586-021-03455-w. [PubMed: 33854236]

(38). Böhringer N; Green R; Liu Y; Mettal U; Marner M; Modaresi SM; Jakob RP; Wuisan ZG; Maier T; Iinishi A; Hiller S; Lewis K; Schäberle TF Mutasynthetic Production and Antimicrobial Characterization of Darobactin Analogs. Microbiol. Spectr 2021, 9 (3), e01535–21. 10.1128/spectrum.01535-21. [PubMed: 34937193]

(39). Haysom SF; Machin J; Whitehouse JM; Horne JE; Fenn K; Ma Y; El Mkami H; Böhringer N; Schäberle TF; Ranson NA; Radford SE; Pliotas C Darobactin B Stabilises a Lateral-Closed Conformation of the BAM Complex in E. Coli Cells. Angew. Chem. Int. ed 2023 62 (34), e202218783. 10.1002/anie.202218783.

(40). Ritzmann N; Manioglu S; Hiller S; Müller DJ Monitoring the Antibiotic Darobactin Modulating the β-Barrel Assembly Factor BamA. Structure 2022, 30 (3), 350–359.e3. 10.1016/j.str.2021.11.004. [PubMed: 34875215]

(41). Seyfert CE; Porten C; Yuan B; Deckarm S; Panter F; Bader CD; Coetzee J; Deschner F; Tehrani KHME; Higgins PG; Seifert H; Marlovits TC; Herrmann J; Müller R Darobactins Exhibiting Superior Antibiotic Activity by Cryo-EM Structure Guided Biosynthetic Engineering. Angew. Chem. Int. Ed 2023, 62 (2), e202214094. 10.1002/anie.202214094.

(42). Peterson JH; Doyle MT; Bernstein HD Small Molecule Antibiotics Inhibit Distinct Stages of Bacterial Outer Membrane Protein Assembly. mBio 2022, 13 (5), e02286–22. 10.1128/mbio.02286-22. [PubMed: 36165532]

(43). Wuisan ZG; Kresna IDM; Böhringer N; Lewis K; Schäberle TF Optimization of Heterologous Darobactin A Expression and Identification of the Minimal Biosynthetic Gene Cluster. Metab. Eng 2021, 66, 123–136. 10.1016/j.ymben.2021.04.007. [PubMed: 33872780]

(44). Groß S; Panter F; Pogorevc D; Seyfert CE; Deckarm S; Bader CD; Herrmann J; Müller R Improved Broad-Spectrum Antibiotics against Gram-Negative Pathogens via Darobactin Biosynthetic Pathway Engineering. Chem. Sci 2021, 12 (35), 11882–11893. 10.1039/D1SC02725E. [PubMed: 34659729]

(45). Fushinobu S; Nishimasu H; Hattori D; Song H-J; Wakagi T Structural Basis for the Bifunctionality of Fructose-1,6-Bisphosphate Aldolase/Phosphatase. Nature 2011, 478 (7370), 538–541. 10.1038/nature10457. [PubMed: 21983966]

(46). Sakaki K; Ohishi K; Shimizu T; Kobayashi I; Mori N; Matsuda K; Tomita T; Watanabe H; Tanaka K; Kuzuyama T; Nishiyama M A Suicide Enzyme Catalyzes Multiple Reactions for Biotin Biosynthesis in Cyanobacteria. Nat. Chem. Biol 2020, 16 (4), 415–422. 10.1038/s41589-019-0461-9. [PubMed: 32042199]

(47). Nguyen H; Made Kresna ID; Böhringer N; Ruel J; Mora E. de la; Kramer J-C; Lewis K; Nicolet Y; Schäberle TF; Yokoyama K Characterization of a Radical SAM Oxygenase for the Ether Crosslinking in Darobactin Biosynthesis. J. Am. Chem. Soc 2022, 144 (41), 18876–18886. 10.1021/jacs.2c05565. [PubMed: 36194754]

(48). Ma S; Xi W; Wang S; Chen H; Guo S; Mo T; Chen W; Deng Z; Chen F; Ding W; Zhang Q Substrate-Controlled Catalysis in the Ether Cross-Link-Forming Radical SAM Enzymes. J. Am. Chem. Soc 2023. 10.1021/jacs.3c04355.

(49). Guo S; Wang S; Ma S; Deng Z; Ding W; Zhang Q Radical SAM-Dependent Ether Crosslink in Daropeptide Biosynthesis. Nat. Commun 2022, 13 (1), 2361. 10.1038/s41467-022-30084-2. [PubMed: 35487921]

(50). Seyfert CE; Müller AV; Walsh DJ; Birkelbach J; Kany AM; Porten C; Yuan B; Krug D; Herrmann J; Marlovits TC; Hirsch AKH; Müller R New Genetically Engineered Derivatives of Antibacterial Darobactins Underpin Their Potential for Antibiotic Development. J. Med. Chem 2023. 10.1021/acs.jmedchem.3c01660.

(51). Böhringer N; Kramer J-C; Mora E. de la; Padva L; Wuisan ZG; Liu Y; Kurz M; Marner M; Nguyen H; Amara P; Yokoyama K; Nicolet Y; Mettal U; Schäberle TF Genome- and Metabolome-Guided Discovery of Marine BamA Inhibitors Revealed a Dedicated Darobactin Halogenase. Cell Chem. Biol 2023, 0 (0). 10.1016/j.chembiol.2023.06.011.

(52). Suckau D; Resemann A; Schuerenberg M; Hufnagel P; Franzen J; Holle A A Novel MALDI LIFT-TOF/TOF Mass Spectrometer for Proteomics. Anal. Bioanal. Chem 2003, 376 (7), 952–965. 10.1007/s00216-003-2057-0. [PubMed: 12830354]

(53). Haft DH; Selengut JD; Richter RA; Harkins D; Basu MK; Beck E TIGRFAMs and Genome Properties in 2013. Nucleic Acids Res. 2013, 41 (Database issue), D387–D395. 10.1093/nar/gks1234. [PubMed: 23197656]

(54). Haft DH; Loftus BJ; Richardson DL; Yang F; Eisen JA; Paulsen IT; White O TIGRFAMs: A Protein Family Resource for the Functional Identification of Proteins. Nucleic Acids Res. 2001, 29 (1), 41–43. 10.1093/nar/29.1.41. [PubMed: 11125044]

(55). Berteau O; Guillot A; Benjdia A; Rabot S A New Type of Bacterial Sulfatase Reveals a Novel Maturation Pathway in Prokaryotes *. J. Biol. Chem 2006, 281 (32), 22464–22470. 10.1074/jbc.M602504200. [PubMed: 16766528]

(56). Grove TL; Ahlum JH; Qin RM; Lanz ND; Radle MI; Krebs C; Booker SJ Further Characterization of Cys-Type and Ser-Type Anaerobic Sulfatase Maturating Enzymes Suggests a Commonality in the Mechanism of Catalysis. Biochemistry 2013, 52 (17), 2874–2887. 10.1021/bi400136u. [PubMed: 23477283]

(57). Appel MJ; Bertozzi CR Formylglycine, a Post-Translationally Generated Residue with Unique Catalytic Capabilities and Biotechnology Applications. ACS Chem. Biol 2015, 10 (1), 72–84. 10.1021/cb500897w. [PubMed: 25514000]

(58). Allen CFH The Identification of Carbonyl Compounds by Use of 2,4-Dinitrophenylhydrazine. J. Am. Chem. Soc 1930, 52 (7), 2955–2959. 10.1021/ja01370a058.

(59). Uchiyama S; Inaba Y; Kunugita N Derivatization of Carbonyl Compounds with 2,4-Dinitrophenylhydrazine and Their Subsequent Determination by High-Performance Liquid Chromatography. J. Chromatogr. B 2011, 879 (17), 1282–1289. 10.1016/j.jchromb.2010.09.028.

(60). Hehre WJ; Ditchfield R; Radom L; Pople JA Molecular Orbital Theory of the Electronic Structure of Organic Compounds. V. Molecular Theory of Bond Separation. J. Am. Chem. Soc 1970, 92 (16), 4796–4801. 10.1021/ja00719a006.

(61). Treyde W; Riedmiller K; Gräter F Bond Dissociation Energies of X–H Bonds in Proteins. RSC Adv. 2022, 12 (53), 34557–34564. 10.1039/D2RA04002F. [PubMed: 36545577]

(62). Minisci F; Bernardi R; Bertini F; Galli R; Perchinummo M Nucleophilic Character of Alkyl Radicals—VI: A New Convenient Selective Alkylation of Heteroaromatic Bases. Tetrahedron 1971, 27 (15), 3575–3579. 10.1016/S0040-4020(01)97768-3.

(63). Proctor RSJ; Phipps RJ Recent Advances in Minisci-Type Reactions. Angew. Chem. Int. Ed 2019, 58 (39), 13666–13699. 10.1002/anie.201900977.

(64). Simonson T; Perahia D; Bricogne G Intramolecular Dielectric Screening in Proteins. J. Mol. Biol 1991, 218 (4), 859–886. 10.1016/0022-2836(91)90273-9. [PubMed: 2023253]

(65). Gilson MK; Honig B Calculation of the Total Electrostatic Energy of a Macromolecular System: Solvation Energies, Binding Energies, and Conformational Analysis. Proteins Struct. Funct. Bioinforma 1988, 4 (1), 7–18. 10.1002/prot.340040104.

(66). Kloosterman AM; Shelton KE; van Wezel GP; Medema MH; Mitchell DA RRE-Finder: A Genome-Mining Tool for Class-Independent RiPP Discovery. mSystems 2020, 5 (5), 10.1128/msystems.00267-20. 10.1128/msystems.00267-20.

(67). Burkhart BJ; Hudson GA; Dunbar KL; Mitchell DA A Prevalent Peptide-Binding Domain Guides Ribosomal Natural Product Biosynthesis. Nat. Chem. Biol 2015, 11 (8), 564–570. 10.1038/nchembio.1856. [PubMed: 26167873]

(68). Evans R; O'Neill M; Pritzel A; Antropova N; Senior A; Green T; Žídek A; Bates R; Blackwell S; Yim J; Ronneberger O; Bodenstein S; Zielinski M; Bridgland A; Potapenko A; Cowie A; Tunyasuvunakool K; Jain R; Clancy E; Kohli P; Jumper J; Hassabis D Protein Complex Prediction with AlphaFold-Multimer. bioRxiv March 10, 2022, p 2021.10.04.463034. 10.1101/2021.10.04.463034.

(69). Jumper J; Evans R; Pritzel A; Green T; Figurnov M; Ronneberger O; Tunyasuvunakool K; Bates R; Žídek A; Potapenko A; Bridgland A; Meyer C; Kohl SAA; Ballard AJ; Cowie A; Romera-Paredes B; Nikolov S; Jain R; Adler J; Back T; Petersen S; Reiman D; Clancy E; Zielinski M; Steinegger M; Pacholska M; Berghammer T; Bodenstein S; Silver D; Vinyals O; Senior AW; Kavukcuoglu K; Kohli P; Hassabis D Highly Accurate Protein Structure Prediction with AlphaFold. Nature 2021, 596 (7873), 583–589. 10.1038/s41586-021-03819-2. [PubMed: 34265844]

(70). Ashkenazy H; Abadi S; Martz E; Chay O; Mayrose I; Pupko T; Ben-Tal N ConSurf 2016: An Improved Methodology to Estimate and Visualize Evolutionary Conservation in Macromolecules. Nucleic Acids Res. 2016, 44 (Web Server issue), W344–W350. 10.1093/nar/gkw408. [PubMed: 27166375]

(71). Bobeica SC; Zhu L; Acedo JZ; Tang W; van der Donk WA Structural Determinants of Macrocyclization in Substrate-Controlled Lanthipeptide Biosynthetic Pathways. Chem. Sci 2020, 11 (47), 12854–12870. 10.1039/D0SC01651A. [PubMed: 34094481]

(72). Le T; Jeanne Dit Fouque K; Santos-Fernandez M; Navo CD; Jiménez-Osés G; Sarksian R; Fernandez-Lima FA; van der Donk WA Substrate Sequence Controls Regioselectivity of Lanthionine Formation by ProcM. J. Am. Chem. Soc 2021, 143 (44), 18733–18743. 10.1021/jacs.1c09370. [PubMed: 34724611]

(73). Tang W; Jiménez-Osés G; Houk KN; van der Donk WA Substrate Control in Stereoselective Lanthionine Biosynthesis. Nat. Chem 2015, 7 (1), 57–64. 10.1038/nchem.2113. [PubMed: 25515891]

(74). Zhu S; Fage CD; Hegemann JD; Yan D; Marahiel MA Dual Substrate-Controlled Kinase Activity Leads to Polyphosphorylated Lasso Peptides. FEBS Lett. 2016, 590 (19), 3323–3334. 10.1002/1873-3468.12386. [PubMed: 27585551]

(75). Ding W; Li Y; Zhang Q Substrate-Controlled Stereochemistry in Natural Product Biosynthesis. ACS Chem. Biol 2015, 10 (7), 1590–1598. 10.1021/acschembio.5b00104. [PubMed: 25844528]

(76). Tang W; Thibodeaux GN; van der Donk WA The Enterococcal Cytolysin Synthetase Coevolves with Substrate for Stereoselective Lanthionine Synthesis. ACS Chem. Biol 2016, 11 (9), 2438–2446. 10.1021/acschembio.6b00397. [PubMed: 27348535]

(77). Lundahl MN; Sarksian R; Yang H; Jodts RJ; Pagnier A; Smith DF; Mosquera MA; van der Donk WA; Hoffman BM; Broderick WE; Broderick JB Mechanism of Radical S-Adenosyl-l-Methionine Adenosylation: Radical Intermediates and the Catalytic Competence of the 5′-Deoxyadenosyl Radical. J. Am. Chem. Soc 2022, 144 (11), 5087–5098. 10.1021/jacs.1c13706. [PubMed: 35258967]

(78). Dong S-H; Liu A; Mahanta N; Mitchell DA; Nair SK Mechanistic Basis for Ribosomal Peptide Backbone Modifications. ACS Cent. Sci 2019, 5 (5), 842–851. 10.1021/acscentsci.9b00124. [PubMed: 31139720]

(79). Blue TC; Davis KM Computational Approaches: An Underutilized Tool in the Quest to Elucidate Radical SAM Dynamics. Molecules 2021, 26 (9), 2590. 10.3390/molecules26092590. [PubMed: 33946806]

(80). Hanževački M; Croft AK; Jäger CM Activation of Glycyl Radical Enzymes—Multiscale Modeling Insights into Catalysis and Radical Control in a Pyruvate Formate-Lyase-Activating Enzyme. J. Chem. Inf. Model 2022, 62 (14), 3401–3414. 10.1021/acs.jcim.2c00362. [PubMed: 35771966]

(81). Wang X; Zhu W; Liu Y Tryptophan Lyase (NosL): Mechanistic Insights into Amine Dehydrogenation and Carboxyl Fragment Migration by QM/MM Calculations. Catal. Sci. Technol 2017, 7 (13), 2846–2856. 10.1039/C7CY00573C.

(82). Pan SJ; Rajniak J; Maksimov MO; Link AJ The Role of a Conserved Threonine Residue in the Leader Peptide of Lasso Peptide Precursors. Chem. Commun 2012, 48 (13), 1880–1882. 10.1039/C2CC17211A.

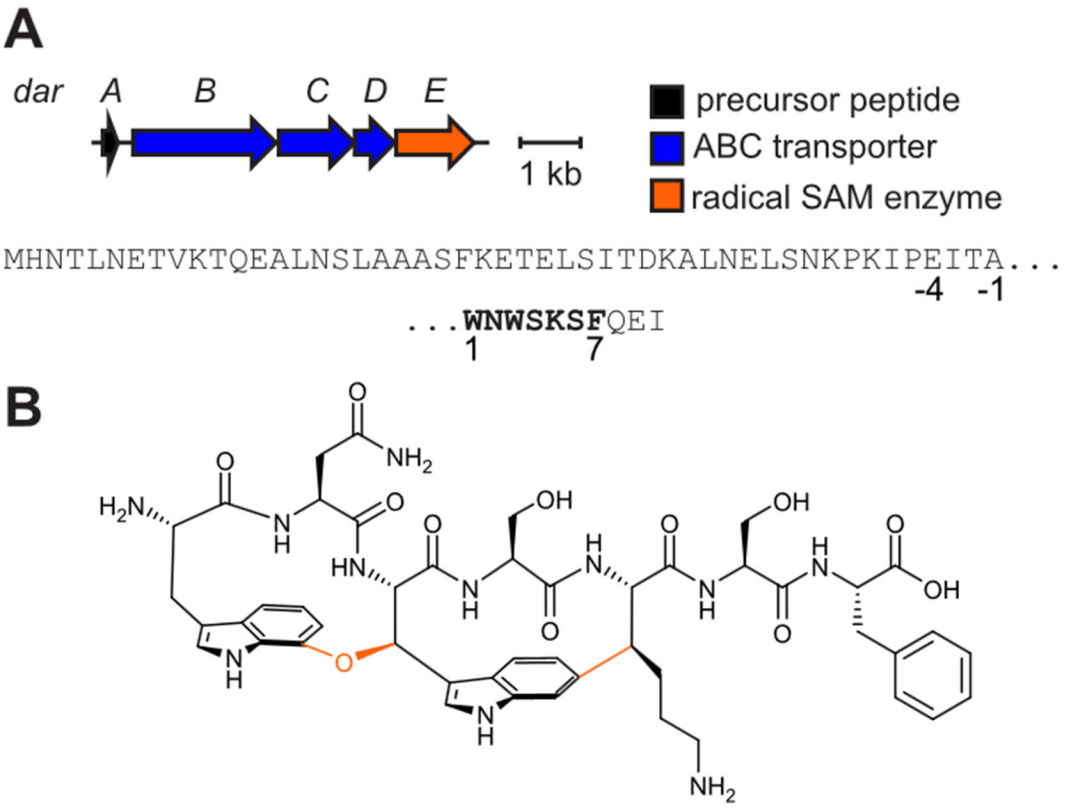

Figure 1: Darobactin BGC and structure.

(A) Darobactin biosynthetic gene cluster (BGC) diagram and DarA sequence. *Top*, sequence of leader region; *bottom*, sequence of heptapeptide core (bold) and Gln-Glu-Ile tripeptide follower sequence. Glu(−4) provides a convenient site for endoproteinase GluC cleavage. (B) Structure of darobactin. Orange bonds and atoms indicate DarE modifications (i.e., Trp1-C7 to Trp3-Cβ ether and Trp3-C6 to Lys5-Cβ C-C).

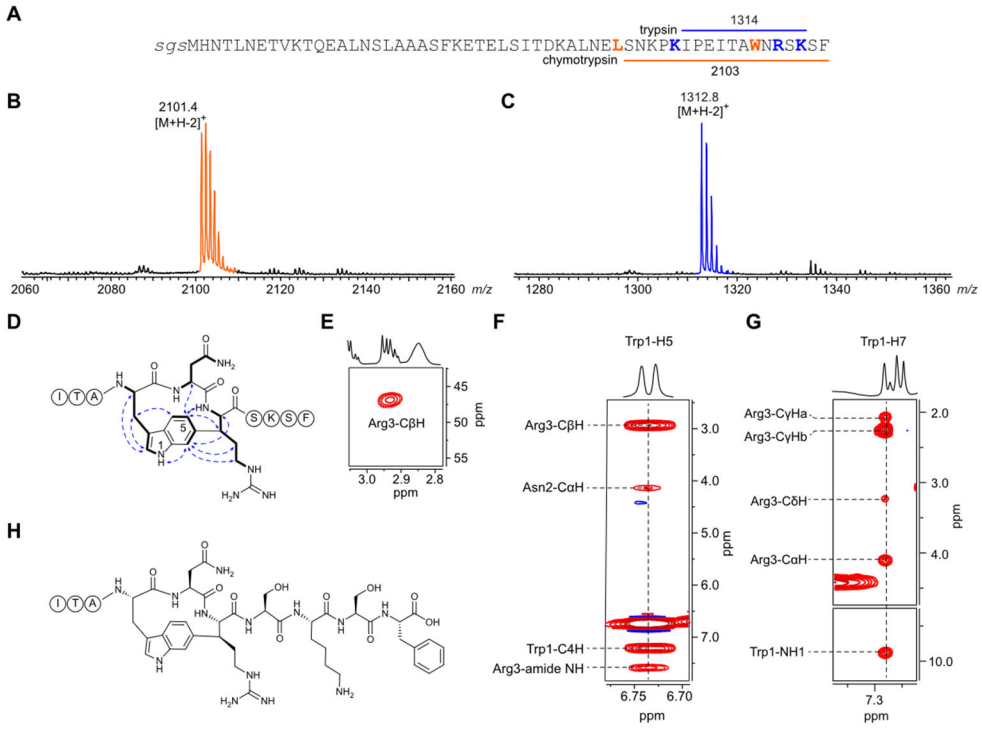

Figure 2: The DarA-W3R variant forms a single Trp1-Arg3 C-C crosslink.

(A) Sequence of TEV protease-cleaved MBP-DarA-W3R variant with the pertinent chymotryptic (orange) and tryptic (blue) peptide fragments and masses indicated. The lowercase and italicized residues (sgs) are not naturally part of DarA. (B-C) MALDI-TOF-MS results of (B) chymotryptic and (C) tryptic digests of DarA-W3R. (D) Diagnostic NMR correlations for the W3R variant confirming a Trp1-Arg3 macrocycle (^{1}H-^{1}H NOESY: blue arrows; ^{1}H-^{1}H TOCSY: thick black lines). (E) ^{1}H-^{13}C HSQC cross peak for Arg3-CβH. (F) Trp1-H5 and (G) Trp1-H7 NOE correlations that establish connectivity and stereochemistry. (H) W3R variant structure with stereochemical configurations shown. Complete structural assignment is provided in the supplemental information (Figures S27-S31, Table S2).

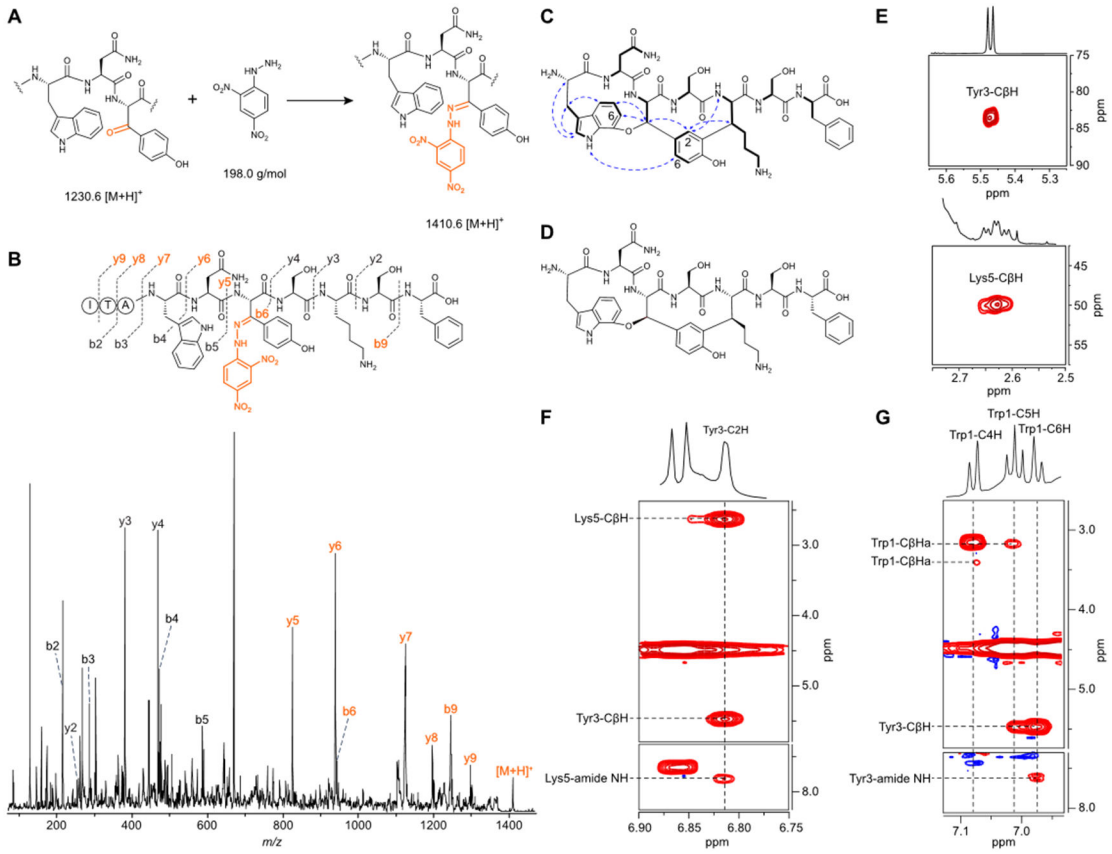

Figure 3: Analysis of a β-oxotyrosine-containing peptide and darobactin W3Y.

(A) Hydrazone formation from the reaction of β-oxotyrosine with 2,4-DNPH. (B) LIFT-MS/MS analysis of the W3Y hydrazone (*m/z* 1410.7) with observed daughter ions indicated. Orange, ions harboring the hydrazone. (C) Structure of darobactin W3Y (^{1}H-^{1}H NOESY: blue arrows; ^{1}H-^{1}H TOCSY: thick black lines). D) Structure of darobactin W3Y with elucidated stereochemical information. (E) ^{1}H-^{13}C HSQC cross peak for Tyr3- and Lys5-CβH. (F) Tyr3 and (G) Trp1 ^{1}H-^{1}H NOESY correlations that establish crosslink connectivity and stereochemistry. Complete structural assignment i*s* provided in the supplemental information (Figures S60-S64, Table S4).

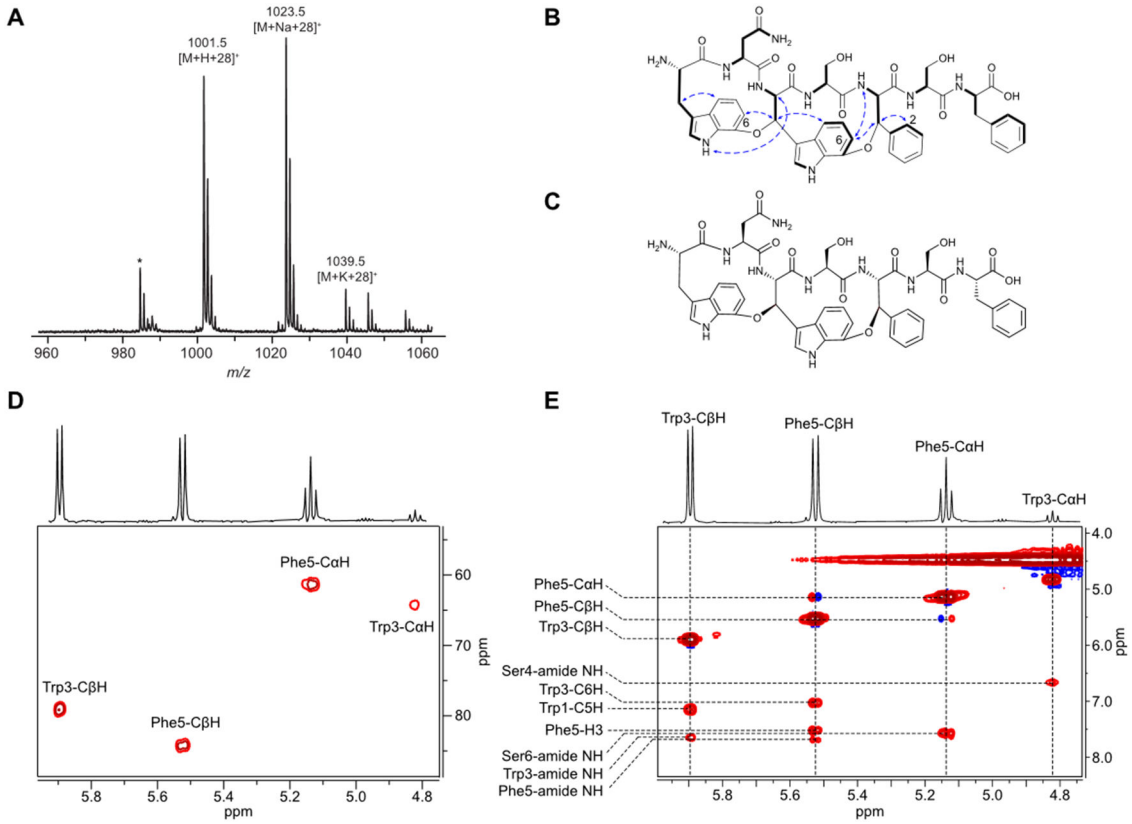

Figure 4: Structural characterization of darobactin K5F.

(A) MALDI-TOF mass spectrum of proteinase K-digested DarA-K5F. * indicates laser-induced deamination. (B) Structure of darobactin K5F (^{1}H-^{1}H NOESY: blue arrows; ^{1}H-^{1}H TOCSY: thick black lines). (C) Structure of darobactin K5F with elucidated stereochemical information. (D) ^{1}H-^{13}C HSQC cross-peaks for the Trp3 and Phe5 CαH and CβH. (E) ^{1}H-^{1}H NOESY correlations that established linkage connectivity and stereochemistry. Complete structural assignment is provided in the supplemental information (Figure S71-S75, Table S5).

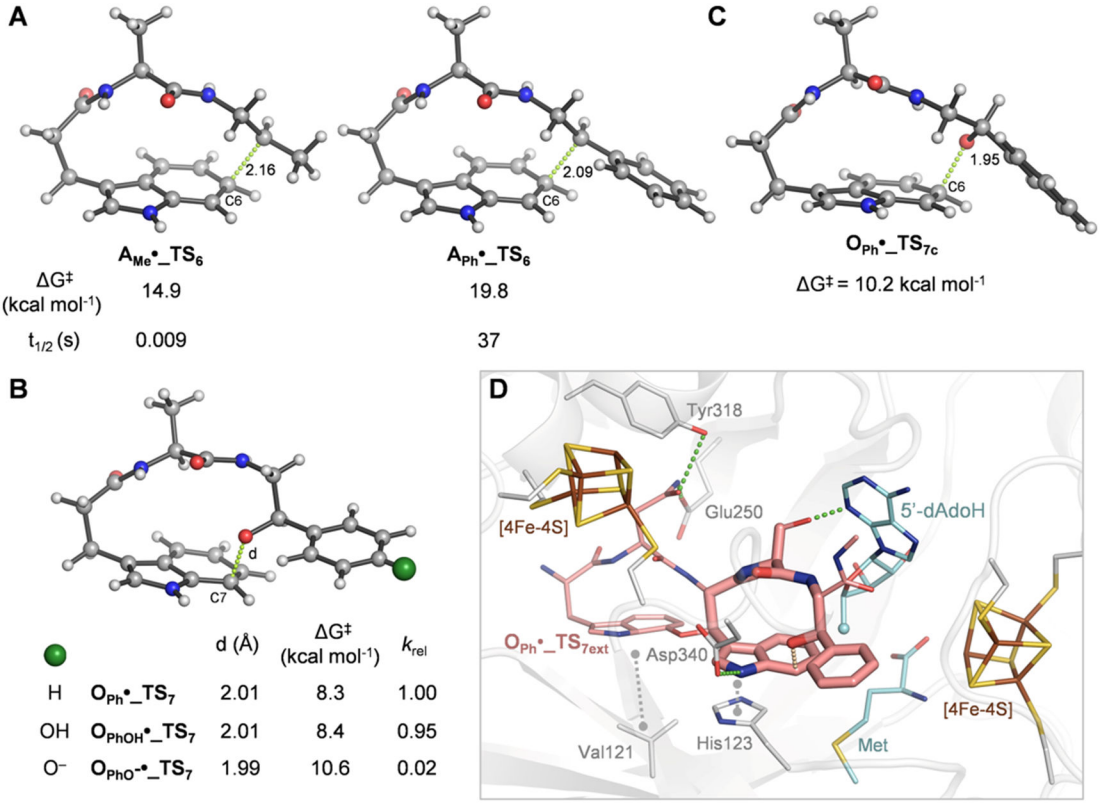

		d (Å)	ΔG‡ (kcal mol-1)	k_{rel}
H	O_{Ph}•_TS_7	2.01	8.3	1.00
OH	O_{PhOH}•_TS_7	2.01	8.4	0.95
O⁻	O_{PhO^-}•_TS_7	1.99	10.6	0.02

Figure 5: Computational Investigation of Crosslink Formation in Darobactin.

(A) QM-optimized transition state structures leading to C-C bond formation at C6 from C-centered alkyl (**A_{Me}•_TS_6**) and aryl (**A_{Ph}•_TS_6**) radicals. The activation barriers (ΔG‡) and half-lives at 25 °C derived from Eyring's equation are given. (B) QM-optimized transition state structures leading to ether formation at C7 from O-centered benzyl (**O_{Ph}•_TS_7**) and *p*-hydroxybenzyl (protonated and deprotonated forms, **O_{PhOH}•_TS_7** and **O_{PhO^-}•_TS_7**, respectively), together with their associated ΔG‡ and relative rate constants (k_{rel}) at 25 °C. (C) Similar to panel B but for **O_{Ph}•_TS_{7c}**. Distances for bond formation are given (Å) and indicated as green dashed lines. (D) Molecular docking of a truncated model of darobactin (pink wireframe), featuring the QM-optimized transition state for ether crosslinking between Trp3-C7 and alkoxy-Phe5 (pink sticks), bound to DarE. 5'-AdoH and Met (cyan, the reacting 5' methyl carbon is shown as a sphere), [4Fe-4S] centers, and relevant active site residues (grey) are shown in wireframe. H-bonds and van der Waals interactions are shown as green and grey dashed lines, respectively.

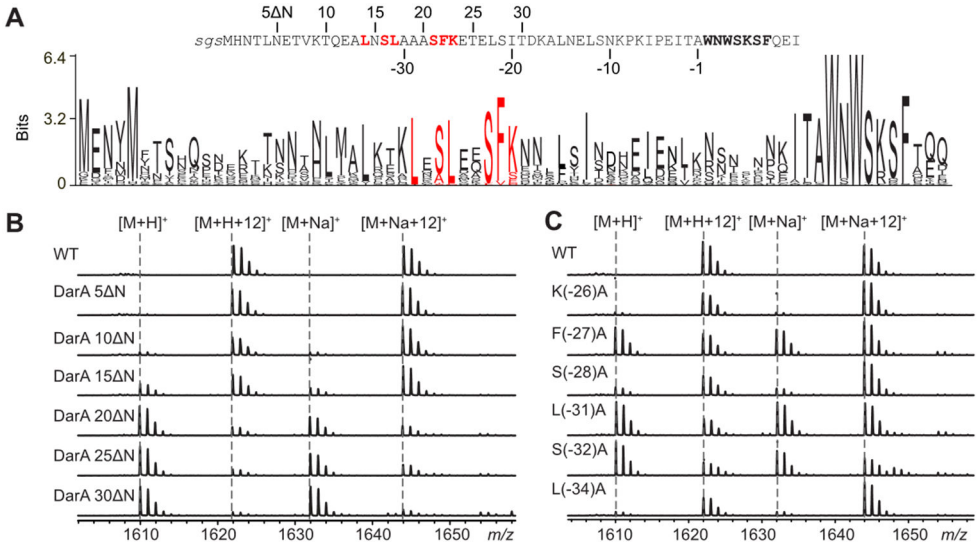

Figure 6: In vivo Characterization of DarA Processing with Leader Variants

(A) Sequence of TEV-protease cleaved DarA with truncation numbering from N-terminus (above sequence) and the conventional negative numbering for leader regions (below sequence) starting from the core sequence (bold). A sequence logo of bioinformatically identified darobactin precursor peptides (n = 148) is shown. Red, conserved positions evaluated by Ala substitution. (B) MALDI-TOF mass spectra of GluC-digested DarA leader truncations after co-expression with DarE. *m/z* 1610 corresponds to unmodified DarA that includes Ile-Thr-Ala and Gln-Glu-Ile from the leader and follower regions, respectively. M+12 ions correspond to the same sequence that includes the ether and C-C crosslinks of mature darobacin. (C) Same as panel B but for Ala-substituted leader variants after co-expression with DarE.